CrossMark

ORIGINAL ARTICLE

Diffusional mass transfer coefficient at the water–sediment interface for wind-induced flow in very shallow lagoons

Alberto de la Fuente[1] · César Ordóñez[1] · Rodrigo Pérez[1]

Abstract Very shallow lagoons that are a few centimeters deep are common in the arid Andes of Northern Chile, Argentina, Bolivia and Perú. The dynamics of these lagoons are dominated by the water–sediment interface (WSI) and strong afternoon winds. Although many studies have examined the diffusional mass transfer coefficients (k_t) of open channel flows, estimates for wind-induced flows are still unknown. The aim of this article is to propose and validate an analytical expression for computing k_t at the WSI for wind-induced flow. The laboratory measurements were conducted in a wind tunnel with a water tank of variable depth located at its downwind end. Natural muddy sediments were placed in the middle of the tank so that the dissolved oxygen (DO) was consumed in the sediments. The diffusional mass transfer coefficient that characterizes the DO uptake in the sediment was obtained from DO micro-profiles measured with an OX-25 Unisense microelectrode. Water velocity profiles were measured with a 2D side-view Sontek acoustic doppler velocimetry (ADV), and the wind shear velocity was computed based on wind velocity profiles that were measured with an Extech hot-wire anemometer. A total of 16 experiments were conducted with different water depths and wind shear stresses. The constants required by the model were determined from these experiments, and the analytical expression was successfully validated by the laboratory observations. The analytical expression obtained for computing k_t was also validated with field observations that were conducted in October, 2012, in Salar del Huasco, Northern Chile (20.274° S, 68.883° W, 3800 m above sea level). The comparison between the observed and predicted values of k_t provides a determination coefficient of $r^2 = 0.48$ and a p value < 0.01. The results show that the value of k_t for wind-induced flow is proportional to the wind shear velocity and the inverse of the Reynolds number of the wind-induced current.

Keywords Diffusional mass transfer coefficient · Wind-induced flow · Very shallow lagoons · Analytical expression validated with experiments and field observations

✉ Alberto de la Fuente
 aldelafu@ing.uchile.cl

[1] Departamento de Ingeniería Civil, Universidad de Chile, Santiago, Chile

🌢 Springer

1 Introduction

Very shallow lagoons that are less than 10 cm deep are found in the highlands of Chile, Bolivia, Perú and Argentina [10, 11, 17]. Locally, these lagoons are called salars, and they support a sensitive ecosystem that is mainly composed of three flamingo species that feed on benthic organisms [13, 35, 36]. Due to the extreme shallowness of these lagoons, the aquatic ecosystem is controlled by the exchanges of heat and mass across the water sediment interface (WSI). Dissolved oxygen (DO) diffusion across the WSI has gained particular attention because this flux is driven by benthic primary production, respiration and biochemical reactions in the sediments, as well as turbulent transport in the water column [2, 11, 12, 16, 26]. Depending on the turbulent intensity, DO flux across the WSI can be limited by mechanic transport across the diffusive boundary layer (where turbulence in the water column is weak), or by the rate of DO uptake/production in the sediments [4, 11, 23, 29].

Without considering a suspended layer of sediments where turbulent eddies promotes vertical transport [18], the WSI is located at $z = 0$, where z is the vertical coordinate and is oriented positive upward (Fig. 1a). The DO flux across the WSI is generally described by the linear transfer law (e.g., [9])

$$J = -D \frac{\partial C}{\partial z}\bigg|_{z=0^+} = -k_t(C_W - C_S) \tag{1}$$

where D denotes the molecular diffusion coefficient, C_W is the concentration outside the diffusive boundary layer, C_S is the concentration at the WSI, and k_t is the diffusional mass transfer coefficient, which is the focus of this paper. k_t is usually defined as D divided by the diffusive boundary layer thickness that depends on the turbulence outside of the diffusive boundary layer [1, 20]. Note that if the DO flux is driven by DO uptake in the sediments, then $J < 0$.

The value of k_t depends on the turbulence intensity above the WSI. Several authors have demonstrated that in open channel flow, the ratio $k_t/(u_{*b}Sc^{-2/3})$ is constant and has values between 1/20 and 1/6 [8, 19, 28, 33]. Here, u_{*b} is the bottom shear velocity, and Sc is the Schmidt number, which is defined as $Sc = v/D$, where v is the kinematic water viscosity. However, the hydrodynamics of very shallow lagoons cannot be represented by open channel flow because the main energy source that drives the flow is not gravity but the wind that blows in the afternoons [10, 11, 21].

The aim of this article is to investigate the relation between the wind shear stress, the wind-induced current and the diffusional mass transfer in a flow as described above. An analytic expression for computing k_t as a function of the wind shear stress (u_*) and the
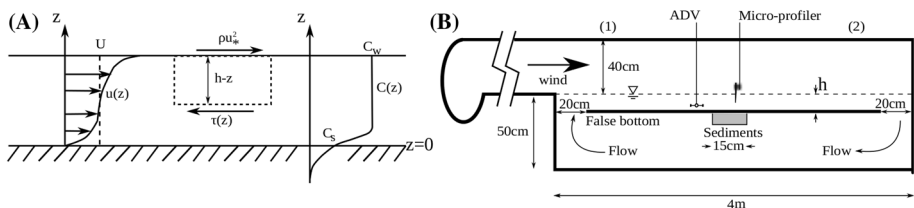
Fig. 1 a Conceptual schematic of the vertical profiles of flow velocity and DO. Sketched velocity profile represents a turbulent Couette flow. **b** Experimental setup

Reynolds number of the wind-induced currents ($Re = Uhv^{-1}$) is first derived. Laboratory measurements allowed us to validate the form of the analytic expression, and to determine the value of the constants involved. This expression is tested against field measurements that were performed in Salar del Huasco, Northern Chile (20.274°S, 68.883°W, 3800 m above sea level), in October, 2012.

2 Theoretical background

2.1 Wind-induced flow

For a turbulent Couette-like flow modified by an opposing horizontal pressure gradient, the force balance in the control volume of height $h - z$ (Fig. 1a) is written as

$$\tau_s - \tau(z) = (h - z)\frac{\partial p}{\partial x} \tag{2}$$

where $\tau_s = \rho u_*^2$ denotes the wind shear stress, u_* is the wind shear velocity over the tank, $\tau(z)$ is the shear stress at elevation z, and p is the pressure. The right side term is the horizontal pressure gradient integrated over the control volume of height $h - z$. The shear stress $\tau(z)$ can be written in terms of the eddy viscosity v_t, and the open channel flow closure [14, 27] was used to describe it as

$$v_t = \kappa u_* \frac{z}{h}(h - z) \tag{3}$$

with $\kappa = 0.41$. The wind shear velocity u_* is used as the characteristic turbulent speed of the flow because the primary source of turbulent kinetic energy is the wind rather than the shear stress on the bottom. An additional discussion of this assumption based on the experimental observations is presented in the following section.

By introducing the wall units scales [27], Eq. 2 can be written in dimensionless form as

$$1 - \alpha\left(1 - \frac{z^+}{h^+}\right) = \left(1 + v_t^+\right)\frac{du^+}{dz^+} \tag{4}$$

where $u^+ = uu_*^{-1}$, $z^+ = u_*zv^{-1}$, $h^+ = u_*hv^{-1}$, and $v_t^+ = v_tv^{-1}$. The coefficient α in Eq. 4 represents the non-dimensional opposing pressure gradient that is generated in response to the wind shear stress such that

$$\frac{\partial p}{\partial x} = \alpha\frac{\rho u_*^2}{h} \tag{5}$$

By evaluating Eq. 4 in z^+, it is obtained that $\alpha = \left(1 - u_{*_b}|u_{*_b}|/u_*^2\right)$, where u_{*_b} denotes the bottom shear stress. Consequently, the case in which $\alpha = 0$ represents turbulent Couette flow, and $\alpha = 1$ describes the flow where the surface shear stress is completely counteracted by the horizontal pressure gradient [32]. Finally, u_{*_b} was written in terms of the average flow speed U as

$$u_{*b}^2 = fU^2 \tag{6}$$

where f denotes the bottom friction coefficient, that can be related to the horizontal pressure gradients as

$$f = \frac{(1 - \alpha)}{U^{+2}} \qquad (7)$$

where $U^+ = U/u_*$.

2.2 Diffusional mass transfer coefficient

An alternative version of Eq. 4 introduces the viscous sub-layer thickness z_o as a boundary condition for the turbulent flow, where $v_t^+ \gg 1$. Using this assumption in Eq. 4 ($v_t^+ + 1 \approx v_t^+$), the following analytical expression for the velocity profile u^+ is obtained as a function of z^+:

$$\kappa u^+ = (1 - \alpha) \ln z^+ - \ln(h^+ - z^+) + c \qquad (8)$$

where c is the integral constant that was obtained by evaluating at $z_0^+ = z_0 u_* v^{-1}$, and the logarithmic velocity is $u^+ = 0$. If z_0^+ is small with respect to h^+, the average flow velocity $U^+ = 1/h^+ \int_0^{h^+} u^+ dz^+$ can be written as

$$\kappa U^+ = (1 - \alpha) \ln\left(\frac{h^+}{z_0^+}\right) + \alpha \qquad (9)$$

The diffusive boundary layer thickness δ_c can be written as proportional to $z_0 Sc^{-1/3}$ [1], so z_0^+ is written in terms of k_t as

$$z_0^+ = \beta \frac{u_*}{k_t} Sc^{-2/3} \qquad (10)$$

where β is a coefficient to be fitted. Finally, Eq. 9 can be written in terms of the friction coefficient of Eq. 6, such that

$$\frac{\kappa}{\sqrt{f}} \sqrt{1 - \alpha} - \alpha + (1 - \alpha) \ln \sqrt{1 - \alpha} = (1 - \alpha) \ln \frac{Re \sqrt{f}}{z_o^+} \qquad (11)$$

where $Re = Uhv^{-1}$ denotes the Reynolds number of the wind-induced current. Then, as it will be shown later, the left-hand side of Eq. 11 can be written as

$$\frac{\kappa}{\sqrt{f}} \sqrt{1 - \alpha} - \alpha + (1 - \alpha) \ln \sqrt{1 - \alpha} \approx (1 - \alpha) \frac{\kappa}{\sqrt{f}} \qquad (12)$$

As a consequence of this simplification, with the definition of Eq. 10, Eq. 11 can be finally written as

$$\frac{k_t}{u_* Sc^{-2/3}} = \frac{\beta}{Re \sqrt{f}} \exp\left(\frac{\kappa}{\sqrt{f}}\right) \qquad (13)$$

3 Methods

3.1 Experimental setup

The experiments were performed in the Francisco Javier Dominguez Hydraulics Laboratory at the Universidad de Chile in a tank that was 4 m long, 0.5 m wide, and 0.5 m deep

located at the downwind end of a wind-tunnel (Fig. 1b). The tank contains a variable depth false bottom with 20-cm-long openings at both the upwind and downwind ends, so water that is dragged by the wind can recirculate below the false bottom. The water depth above the false bottom, h, can vary between 3 and 9 cm. In the middle of the false bottom, a 0.15-m-long compartment was filled with muddy sediments (Fig. 1b) to induce DO uptake, which provides the necessary conditions to measure the diffusive boundary layer (see Fig. 1a). Steady-state conditions were achieved by the balance between the sediment oxygen demand and reaeration across the air–water interface. Muddy sediments were collected from the artificial lagoon in O'Higgins Park near the university campus in Santiago, Chile. Prior to being installed in the experimental facility, the sediments were cleaned of gravel and debris to prevent breaking the microelectrodes. Before the experiments, the surface of the sediments was smoothed to the same elevation as the false bottom.

A total of 16 experiments were conducted. Each was characterized by the water depth h above the false bottom and the wind shear velocity u_*. The wind shear velocity varied between 0.25 and 1 cm s^{-1}. Table 1 summarizes the experimental conditions and the results of the 16 experiments. Several measurements were performed from each experiment, which were defined in terms of h and u_*. First, vertical profiles of the wind speed were measured with an Extech hot-wire anemometer at locations [1] and [2] in Fig. 1B. Location [1] is located 140 cm upstream from the sediments, and location [2] is located 80 cm downstream from the sediments. Each wind velocity profile was constructed with measurements taken every 2 cm starting 1 cm above the mean water level. At each elevation, the anemometer sampling rate was set to 0.2 Hz, and the wind speed was determined by averaging 30 s of measurements. Second, the vertical profile of the water velocity was measured using a 2D side-view Sontek Acoustic Doppler Velocimetry (ADV) approximately 30 cm upwind from the sediment compartment. The vertical spacing was from 3 to 5 mm depending on the water depth, and each vertical profile was constructed from 16 measurements. At each elevation, the corresponding horizontal velocity was computed as the temporal average of 120 s of measurements at a sampling rate of 50 Hz. Note that because of the shallowness of the flow, the ADV instrument was not able to measure vertical velocity. Consequently, it was not possible to measure vertical profiles of the turbulent shear stress.

Finally, in each experiment, three DO micro-profiles were measured at 3, 7.5 and 12 cm from the upwind end of the sediment compartment. These three points were used to determine the presence of effects that can be attributed to the longitudinal growth of the diffusive boundary layer along the streamline. The DO micro-profiles on both sides of the WSI were measured using an OX-25 microprobe with an outer tip of 25 μm that was connected to a Microsensor Multimeter Unisense signal amplifier. Because the thickness of the diffusive sub-layer in our experiments was between 0.5 and 2.3 mm, the vertical spacing of the DO micro-profiles was set to 160 μm to obtain more than 3 observations from within the diffusive sub-layer. It is important to notice that this value is characteristic for our experimental conditions, and should not considered universal since diffusive boundary layers of 0.1 mm thick has been previously reported [4, 23]. The accuracy of the vertical displacement was provided by a semi-automatic motor that moves the sensor at a step size of 80 μm. The sampling rate of the DO microelectrode was 1 Hz, and the DO concentration used for the micro-profile was the temporal average of 10 s of measurements.

Table 1 Summary of the experiments. The values of k_t correspond to the average values of k_{tw} and k_{ts} measured at three locations along the streamline with the corresponding standard deviation, and z_0^+ was computed with $\beta = 0.06$

RUN	h (cm)	u_* (mm s^{-1})	T (°C)	$v \times 10^6$ (m^2 s^{-1})	J (gO$_2$ m^{-2} d^{-1})	C_W (gO$_2$ m^{-3})	C_{WSI} (gO$_2$ m^{-3})	S (gO$_2$ m^{-1} d^{-2})
1	3	5.3	17.2	1.083	0.31	8.46	6.67	0.0110
2	3	8.9	18.62	1.044	0.31	8.38	6.66	0.0117
3	3	9.8	17.26	1.081	0.16	8.56	6.89	0.0018
4	3	12.3	18.28	1.047	0.22	8.19	6.43	0.0051
5	5	4	18.6	1.046	0.50	8.38	5.90	0.0429
6	5	7.6	18.59	1.047	0.31	8.42	6.91	0.0140
7	5	10.7	18.84	1.038	0.14	8.42	7.18	0.0025
8	5	11.8	19.61	1.013	0.24	8.35	6.36	0.0118
9	7	3.6	18.21	1.055	0.43	8.34	5.79	0.0367
10	7	7.1	18.39	1.049	0.35	8.39	6.37	0.0174
11	7	8.5	18.88	1.029	0.21	8.27	7.15	0.0093
12	7	13.1	17.67	1.069	0.17	8.51	7.05	0.0030
13	9	5.6	16.43	1.103	0.39	8.51	6.22	0.0299
14	9	10	16.72	1.095	0.21	8.40	6.63	0.0044
15	9	12	17.07	1.082	0.21	8.30	6.90	0.0063
16	9	14.1	16.97	1.089	0.22	8.74	7.40	0.0096

RUN	Sc (cm s^{-1})	U (cm s^{-1})	α (–)	k_t (m d^{-1})	Re (–)	z_0^+ (–)	h^+ (–)
1	598.8	3.74	0.312	0.204 ± 0.048	1037	1.9	146
2	554.8	6.13	0.444	0.228 ± 0.055	1761	3.0	256
3	596.9	8.50	0.243	0.193 ± 0.018	2358	3.7	271
4	564.9	12.92	0.096	0.170 ± 0.056	3702	5.5	353
5	555.4	1.29	0.858	0.178 ± 0.010	618	1.7	193
6	555.7	2.33	0.903	0.198 ± 0.013	1113	2.9	363
7	548.5	3.50	0.891	0.213 ± 0.036	1686	3.9	513
8	526.5	4.76	0.819	0.249 ± 0.007	2353	3.8	581
9	567.0	1.01	0.921	0.176 ± 0.011	672	1.6	242
10	561.6	2.53	0.858	0.228 ± 0.022	1687	2.4	471
11	547.7	3.61	0.801	0.167 ± 0.010	2455	3.9	581
12	583.8	5.65	0.807	0.176 ± 0.019	3704	5.5	859
13	624.3	1.64	0.924	0.156 ± 0.025	1337	2.5	456
14	614.7	2.54	0.972	0.214 ± 0.024	2091	3.4	825
15	603.0	3.42	0.945	0.176 ± 0.036	2848	5.0	999
16	606.4	4.43	0.921	0.145 ± 0.007	3667	7.0	1169

3.2 Data processing: wind and water velocity

Following the methodology detailed in Thais and Magnaudet [34], the wind shear velocity w_* was obtained by fitting a log-law velocity profile to the measurements. Figure 2a shows an example of a logarithmic profile fitted to the wind-speed measurements at locations [1,
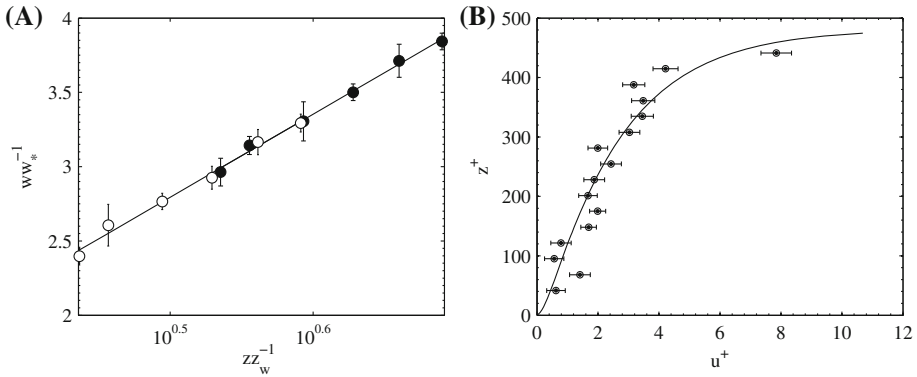
Fig. 2 a Vertical wind velocity profiles. The black circles correspond to the profile measured at location [1] in Fig. 1b, and the white circles correspond to the profile measured at location [2] in Fig. 1b. z_w and w_* denote the water roughness and wind shear velocity, respectively; both obtained with the logarithmic fit of wind velocity profile. **b** Wind-induced velocity profile. The circles correspond to measurements, and the solid line represents the fitted profile. The plotted information is from experiment 13 (Table 1), in which $h = 9$ cm and $u_* = 5.6$ mm s^{-1}. *Error bars* indicates standard deviation of the velocity time-series

2] that correspond to the experiment with $h = 3$ cm and $u_* = 2.9$ mm s^{-1}. The mean shear stress over the channel was then computed by averaging the values of w_*^2 that were obtained at locations (1) and (2). Finally, the shear stress continuity at the air–water interface allows the wind shear velocity on the waterside of the interface, u_*, to be calculated from $u_* = w_* \sqrt{\rho_a/\rho}$, where ρ_a denotes the air density.

The water velocity was described by Eq. 4, where the unknown variable is α. A no-slip boundary condition at $z = 0$ was used to solve Eq. 4, and the obtained velocity profile was fitted to the measurements by changing the value of α. Figure 2b shows the velocity profile that was fitted to the measurements that correspond to $h = 9$ cm and $u_* = 5.6$ mm s^{-1}. The head of the ADV instrument is a cylinder of 15.6 mm of diameter, which imposes that the nearest measurements to the WSI and the free surface are at 7.8 mm away from them. As a consequence, the average of the ADV measurements is not necessarily representative of the vertically-averaged horizontal flow velocity, U. As a consequence, U is hereinafter referred as the vertical average flow velocity computed with the fitted α and the observed u_*.

3.3 Data processing: DO micro-profiles

The DO micro-profiles were analyzed on both sides of the WSI following de la Fuente [11, 12] and Ordoñez et al. [29] to obtain the diffusional mass transfer coefficient. First, the location of the WSI was required, for which the vertical gradient of C at the *ith* point of the micro-profile was computed with a linear fit to the 4 measurements located above the *ith* point of the micro profile. Then, the vertical profile of $\partial C/\partial z$ was obtained, and the WSI was identified by the point at which $\partial C/\partial z$ was a maximum. Examples of these vertical profiles of $\partial C/\partial z$ are shown in Fig. 3a, d while Fig. 3b, e shows the corresponding vertical profile of C. On the water-side of the WSI, the vertical gradient of C at the WSI ($\partial C/\partial z|_{z=0^+}$) was multiplied by D for obtaining the DO flux across the WSI (J, Eq. 1). The corresponding diffusional mass transfer coefficient, k_{tw}, was computed as
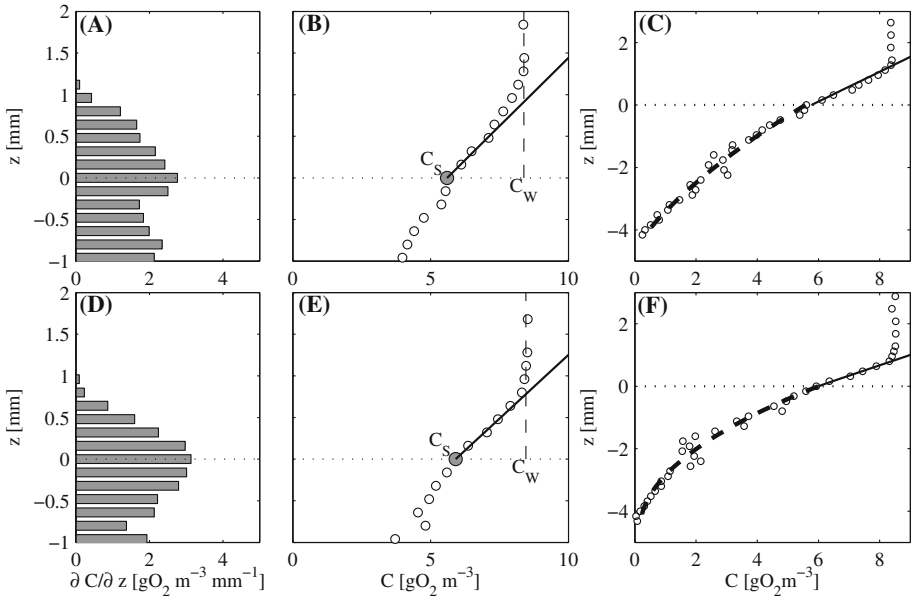
Fig. 3 Example of micro-profile processing. **a, d** vertical profile of $\partial C/\partial z$. **b, e** DO micro-profile near the WSI, including obtained values of C_s and C_W, and linear fit that defines vertical gradient of C required for Eq. 1. **c, f** entire DO micro-profile, including quadratic fit in the sediments for obtaining S (Eq. 16). **a–c** correspond to experiment with $h = 3$ cm, $u_* = 8.9$ mm s^{-1} and the micro-profile taken at 7.5 cm from the upwind end of the sediment compartment. **d–f** to experiment with $h = 9$ cm and $u_* = 5.6$ mm s^{-1}, and the micro-profile taken 7.5 cm from the upwind end of the sediment compartment

$$k_{tw} = \frac{D}{(C_W - C_S)} \left.\frac{\partial C}{\partial z}\right|_{z=0^+} = \frac{-J}{(C_W - C_S)} \tag{14}$$

where C_S (grey circle in Fig. 3b, e) was computing by evaluating the linear fit that provided $\partial C/\partial z|_{z=0^+}$ at the WSI ($z = 0$).

On the sediment side of the WSI, the problem is described by the diffusion-uptake equation, which is written as [5, 22, 31]:

$$D_{ef}\frac{\partial^2 C}{\partial z^2} = r(z) \tag{15}$$

where $r(z)$ denotes the rate of DO uptake per unit of sediment volume, $D_{ef} < D$ is the effective oxygen diffusivity in the sediments that depends on the sediment porosity [5, 30]. Previous studies showed that $r(z)$ can be assumed to be homogeneous in the upper layer of the sediments (i.e., $r(z) = \bar{r}$; [5, 22, 30]. Consequently, the DO concentrations in the sediments are described by a parabolic function [6]. A parabolic function of the form $C(z) = az^2 + bz + C_s$ was then fitted to the DO concentrations within the sediments to obtain $\bar{r} = 2D_{ef}a$. The coupling across the WSI was introduced by forcing $C = C_s$ at the interface, where C_s is the same concentration required to compute J on the water side (grey circle in Fig. 3b, e). Finally, the flux at the sediment side of the WSI can be written as:

$$J = -D_{ef}\left.\frac{\partial C}{\partial z}\right|_{z=0^-} = -\sqrt{SC_S} \tag{16}$$

where $S = 2\bar{r}D_{ef}$ [11, 12] and the diffusional mass transfer coefficient that is measured by considering the processes in the sediments is written as

$$k_{ts} = \frac{\sqrt{SC_S}}{(C_W - C_s)} \qquad (17)$$

According to the flux continuity at the WSI, k_{ts} of Eq. 17 should be equal to k_{tw} from Eq. 14 if the micro-profiles were correctly processed. Figure 3C, F show the processing of two DO micro-profiles, where the solid line shows the linear fit of the water side of the WSI, and dashed line the parabolic fit for obtaining S. Furthermore, flux continuity at the WSI provides that J can be estimated

$$J = \frac{S}{2k_t}\left(-1 + \sqrt{1 + \frac{4k_t^2 C_W}{S}}\right) \qquad (18)$$

Equation 18 is obtained by writing $C_s = J^2/S$ (Eq. 16), and by replacing it into Eq. 1. Equation 18 can also be written as

$$\frac{J}{k_t} = C_W - \frac{J^2}{S} \qquad (19)$$

which shows that in the limit where the biochemical action in the sediments is fast (S is large), $J \approx k_t C_W$ then, the DO flux across the WSI is controlled by k_t; on the contrary, when turbulent transport across the diffusive boundary layer is very efficient (k_t is large), $J \approx \sqrt{SC_W}$ that correspond to the limit when DO flux across the WSI is controlled by biochemical processes in the sediment side of the WSI.

The effective diffusion coefficient in the sediment was computed based on the DO flux continuity at the WSI, which provides that the vertical gradients of C above (at $z = 0^+$) and below (at $z = 0^-$) the WSI are related to each other as

$$D_{ef}\frac{\partial C}{\partial z}\bigg|_{z=0^-} = D\frac{\partial C}{\partial z}\bigg|_{z=0^+} \qquad (20)$$

The vertical gradients of C at $z = 0^-$ and $z = 0^+$ were then computed with a linear fit using three consecutive points below and above the interface, respectively. A linear fit was then used to estimate the D_{ef} as $D_{ef} = (0.85 \pm 0.11)D$, where the error in the estimation is the 95 % confidence interval of the fitted parameter. Since D_{ef} can be assumed proportional to the square of the upper sediments porosity (ϕ, [5]), this estimation ($\phi \approx \sqrt{0.85} = 0.92$) is consistent with previous studies that determined the porosity of the upper sediment layer to be between $\phi = 0.9$ and 0.95 (e.g. [5]).

4 Results

4.1 Wind-induced flow

The intensity of the wind-induced turbulence can be characterized by examining the fluctuations of the horizontal velocity u_{rms} with respect to the average velocity. The vertical profiles of $u_{rms}u_*^{-1}$ are shown in Fig. 4a and show that $u_{rms}u_*^{-1}$ can be assumed to
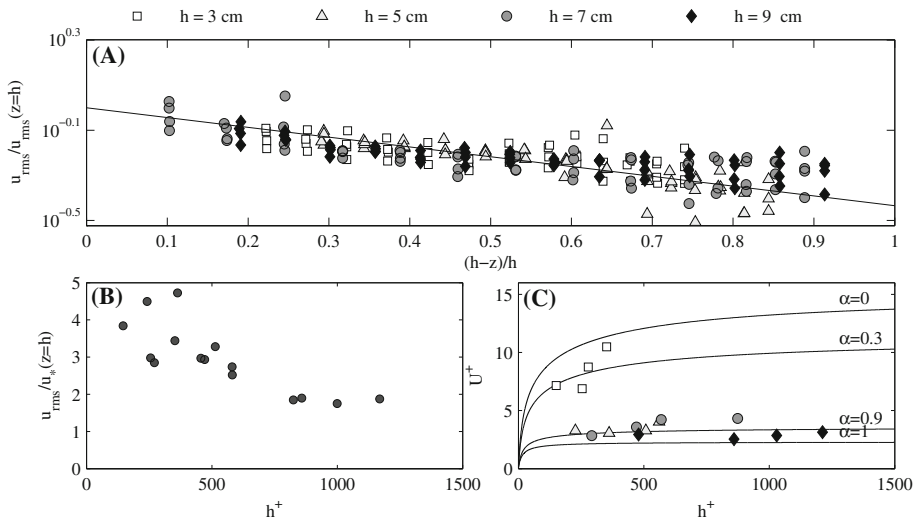
Fig. 4 **a** Vertical profile of $u_{rms}u_*^{-1}$ with respect to the non-dimensional distance to the free surface. The *solid line* shows the fitted profile. Each point correspond to one flow velocity time-series obtained with the ADV. **b** $u_{rms}u_*^{-1}$ evaluated at the free surface as a function of h^+. **c** Non-dimensional mean velocity U^+ with respect to h^+. The *solid line* show the analytical solution obtained by integrating Eq. 4 for the values of α that are shown on the *right side* of the panel C

exponentially decay with the dimensionless distance to the free surface ($u_{rms}u_*^{-1} \propto \exp(-(h-z)/h)$; Fig. 4a). Similar to open channel flows, the ratio $u_{rms}u_*^{-1}$ decreases with the non-dimensional distance to the boundary at which the turbulent kinetic energy is produced; that is, the solid wall in open channel flows [27] and the free surface in wind-induced flow. However, contrary to open channel flows, the $u_{rms}u_*^{-1}$ at the free surface is not a constant [27], and accordingly to Fig. 4b, it decreases with $h^+ = u_*h/\nu$. As a consequence of this result, the wind shear velocity is the characteristic turbulent velocity scale rather than the bottom shear velocity, and it is because the wind shear stress is the main source of turbulent kinetic energy. This behavior is consistent with previous laboratory experiments (e.g., [24]).

Figure 4C shows the vertical averaged water velocity U_{ADV} measured with the ADV normalized by u_* ($U_{ADV}^+ = U/u_*$) as a function of h^+ for each experiment. Note that U_{ADV}^+ is not equal to the vertical average velocity, because the ADV instrument is unable to measure near the bottom and the free surface. The solid lines in Fig. 4c were computed using Eq. 4 for the corresponding values of α indicated on the right hand side. The measurements show that the wind-driven flow is not represented by the turbulent Couette flow, which is given by the curve $\alpha = 0$. On the other hand, the results indicate that the flow is strongly controlled by the opposing pressure gradient and that the influence increases with depth (see Eq. 5). This means that the bottom shear stress is almost negligible for all of the configurations except for $h = 3$ cm, where α was close to 0.3. Finally, the fitted values of α show that in the experimental facility, the bottom shear stress is more important for the shallowest flow. To understand this trend, it must be recognized that the horizontal pressure gradient that acts against the wind, is responsible to drive the water recirculation below the false bottom. Consequently, as h increases, the wind-dragged water volume (Uh) increases (see column Re in Table 1), and a larger pressure gradient is required.

Finally, to quantify the influence of wind-induced waves, the power spectrum of the u_{rms} velocity was computed for all of the flow-velocity time series. This analysis identified the existence of an oscillatory pattern that could be attributed to wind-waves [11]. Figure 5 shows the power spectrum decompositions (PSDs) of the experiments with $h = 3$ cm (left panels) and 9 cm (right panels) and different wind shear stresses. The vertical axis corresponds to the elevation z/h, while the horizontal axis shows the spectral frequency. Figure 5 shows that although the flow velocity field (black triangles) is influenced by wind-induced waves, this influence is restricted to the surface and larger wind stresses. For example, Fig. 5d shows the presence of a clear spectral maximum at a frequency of 2.5 Hz (period of 0.4 s) near the surface ($z/h \gtrsim 0.5$) in the experiments with $h = 3$ cm. This spectral maximum can be attributed to wind-induced waves and was also observed for $h = 9$ cm in a confined area ($z/h \gtrsim 0.8$) (Fig. 5H). These clear oscillatory patterns disappear with depth, which indicates that the measured values of k_t are not influenced by wind-induced waves.
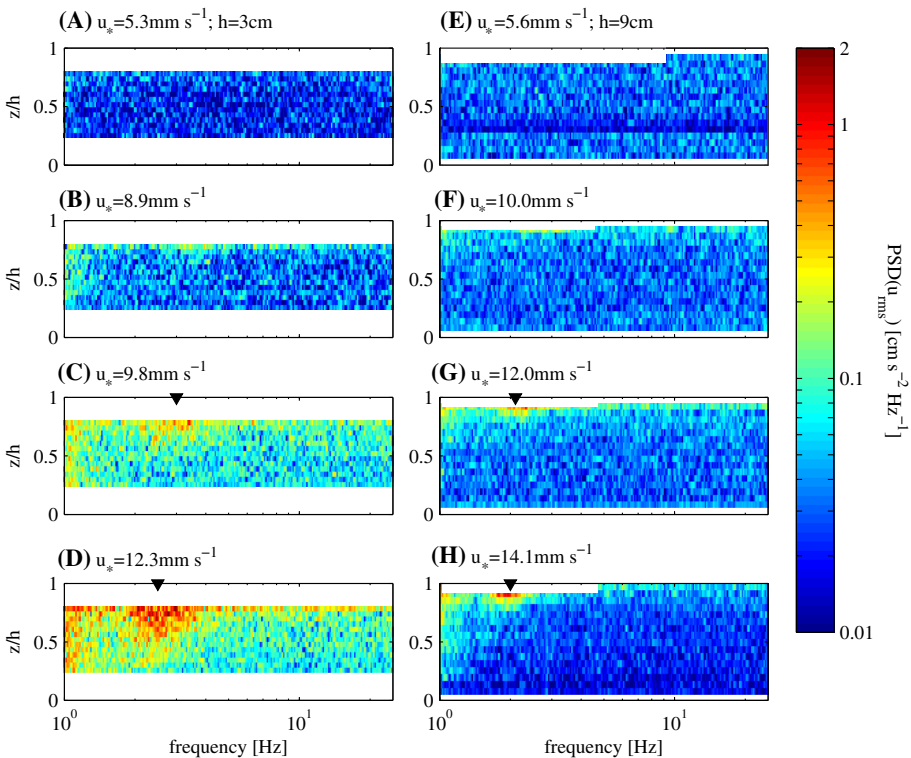

Fig. 5 Contour plots of the power spectrum decomposition of u_{rms} as a function of the dimensionless elevation (*vertical axis*) and frequency (*horizontal axis*). The *black triangles* indicate the presence of a wave-induced velocity pattern. **a**–**d** correspond to experiments 1 to 4, respectively, and **e**–**h** correspond to experiments 13 to 16, respectively (Table 1)

4.2 Diffusional mass transfer coefficient

Two different diffusional mass transfer coefficients were computed for each DO micro-profile (k_{tw} and k_{ts}). Figure 6a shows a direct comparison between them, where both coefficients were scaled by $u_*Sc^{-2/3}$. There is a good agreement between k_{tw} and k_{ts} with a least squares difference of 0.007 (dashed lines in Fig. 6a); this indicates that the processing methodology of the micro-profiles provided valid results. Bryant et al. [5] showed that depending on the method that is used to process the micro-profiles, the computed DO flux across the WSI varies by approximately 30 % with respect to the average. Consequently, the differences between k_{tw} and k_{ts} shown in Fig. 6a can be considered to be normal, and the average of k_{tw} and k_{ts} is considered to be the representative value of k_t for the corresponding micro-profile.

The theoretical background adopted in this article does not consider the influence of the longitudinal growth of the diffusive boundary layer. In terms of the diffusional mass transfer coefficient, the growth of the diffusive boundary layer thickness would be reflected by a reduction of k_t along the streamlines. This assumption was tested by measuring DO-micro profiles 3, 7.5 and 12 cm from the upwind end of the sediment compartment. Figure 6b, c shows the measured values of $k_t/(u_*Sc^{-2/3})$ and J for different locations along the longitudinal axis. Figures 6b, c shows no significantly influence of the micro-profile position on the measured value of k_t. This conclusion can be quantified with the ratios between $k_t/(u_*Sc^{-2/3})$ and the spatial average value of $k_t/(u_*Sc^{-2/3})$ of 1.05 ± 0.15 at 3 cm, 1.00 ± 0.13 at 7.5 cm, and 0.95 ± 0.12 at 12 cm. Similar values are obtained for J. Although these results suggest that the longitudinal position influences the value of $k_t/(u_*Sc^{-2/3})$ or J, the standard deviation of these values is much larger than the difference between them. Consequently, we conclude that x does not produce significant difference on
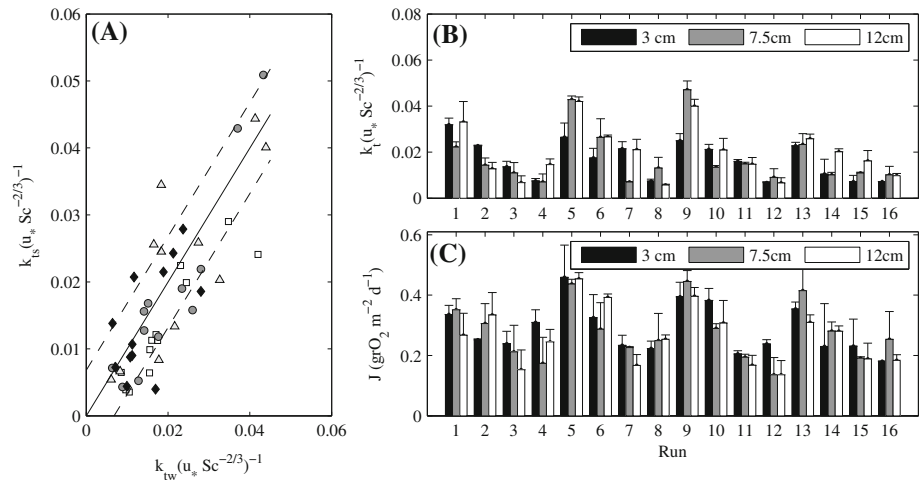
Fig. 6 **a** Comparison between the measured diffusional mass transfer coefficients by considering the processes on the waterside (k_{tw}) and the sediment side (k_{ts}) of the WSI. **b** Average k_t between k_{tw} and k_{ts} as a function of the experimental conditions and location along the streamlines. The *error bars* correspond to the absolute differences between k_t and k_{tw}. **c** Average J computed with Eq. 1 and 16, a as a function of the experimental conditions and location along the streamlines. The *error bars* correspond to the absolute differences between average J and J computed with Eq. 1

the measured value of $k_t/(u_* Sc^{-2/3})$. The diffusive boundary layer is driven by the wind turbulent kinetic energy and not by the bottom shear stress as in open channel flows.

According to Eq. 9, the average flow velocity induced by the wind depends on the wind shear velocity, h^+, α, and the hydrodynamic bottom roughness, which is linked to the diffusional mass transfer coefficient as $z_0^+ = \beta u_* Sc^{-2/3} k_t^{-1}$. Equation 9 was then fitted to the observed values of U^+ to obtain the value of the coefficient β that is required to compute z_0^+, which resulted in $\beta = 1/(18.6 \pm 5.1)$ (Fig. 7a). With $\beta = 1/18.6$, the skill score (ss) of the estimation of U^+ with Eq. 9 is $ss = 0.95$, and the correlation coefficient $r = 0.99$ [25].

The average value of k_t measured at different locations along the longitudinal profiles (Fig. 6) was used in Fig. 7a. Based on this result (Fig. 7a), the hydrodynamic bottom roughness thickness (z_0) and the diffusional mass transfer coefficient can be related as shown in Eq. 10. The friction coefficient f of Eq. 6 or 7 is required to do this, and our measurements indicate that f is not sensitive to the flow properties (Re and h). This result is shown in Fig. 7b, which plots the square of the bottom friction velocity, $u_{*b}^2 = u_*^2(1 - \alpha)$ (see Eq. 7), against U^2 for all of the experiments. This gives $f = (9.7 \pm 1.4) \times 10^{-3}$ with a skill score $ss = 0.97$ and a correlation coefficient $r = 0.99$.
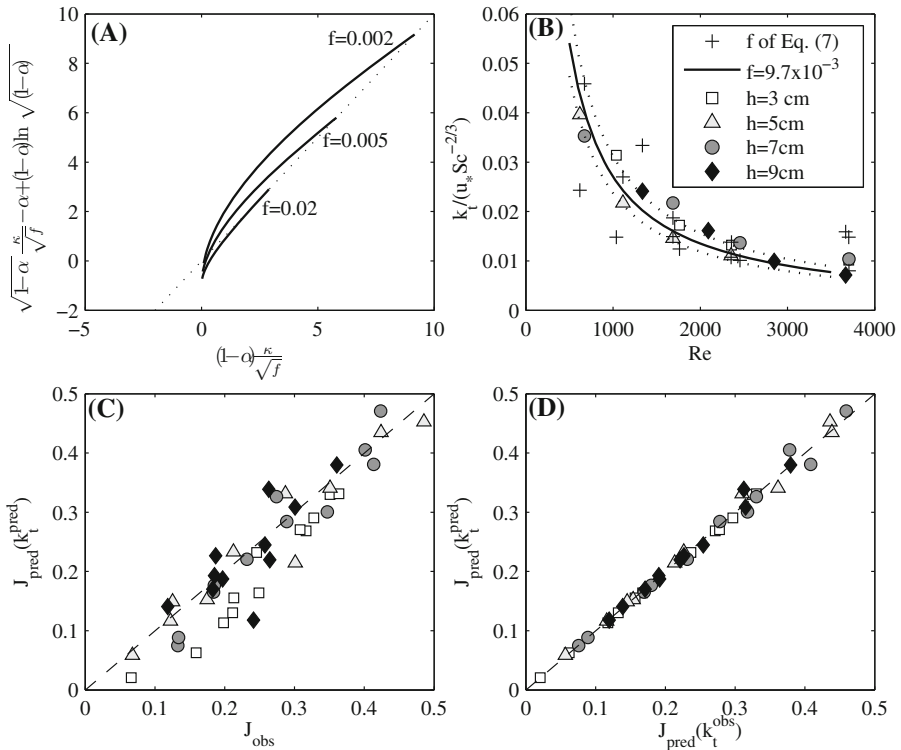
4.3 Prediction of k_t

Accordingly to the previous results, Eq. 9 can be used to predict the value of the k_t. However, the direct use of Eq. 9 to compute z_0^+ amplifies the numerical influence of α when this coefficient approaches 1. This is because $z_0^+ \propto \exp\left(-\frac{1}{\sqrt{1-\alpha}}\right)$. In this context, the validity of the simplification of Eq. 12 was verified in Fig. 8A, where the left hand side of Eq. 12 was plotted against the right hand side of Eq. 12 for different values of α between 0 and 0.99, and f between 0.002 and 0.02. Consequently, Fig. 8a shows that it possible to use Eq. 13 to compute k_t as a function of the friction coefficient and the Reynolds number.

Figure 8b tests the validity of using Eq. 13 to compute $k_t/(u_* Sc^{-2/3})$ as a function of the Reynolds number and the friction coefficient. The coefficients $f = (9.7 \pm 1.4) \times 10^{-3}$ and
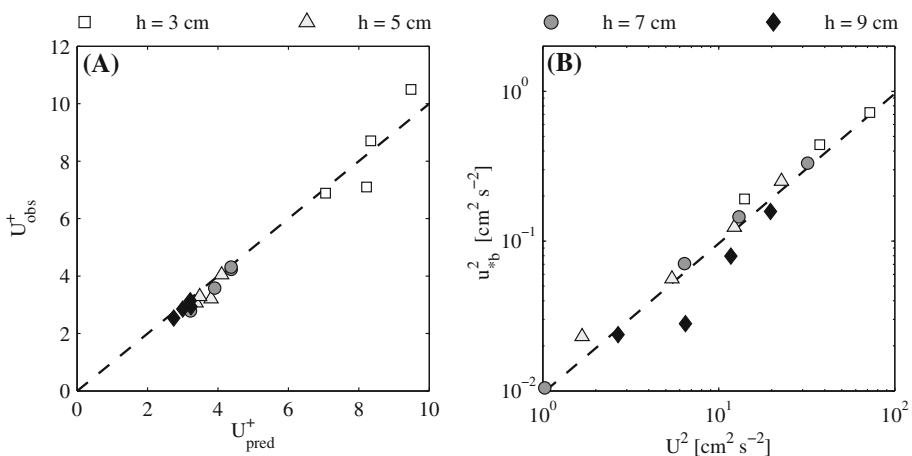
Fig. 7 a Comparison between the observed and predicted values of U^+ with Eq. 9 and $\beta = 1/18.6$. **b** Comparison between square of the bottom shear velocity and U^2. The slope corresponds to the bottom friction coefficient (Eq. 6)

Fig. 8 **a** Test of validity of simplification of Eq. 12. **b** Values of k_t predicted using Eq. 13 and $\beta = 1/18.6$ determined in Fig. 7a and $f = 9.7 \times 10^{-3}$ determined in Fig. 7b. Marks *plus* indicate predicted k_t with Eq. 13 and friction coefficients computed with Eq. 7. **c** Comparison between observed and predicted J using Eq. 18 and Eq. 13. Comparison between predicted J with Eq. 18 using predicted k_t with Eq. 13 ($J_{pred}(k_t^{pred})$) and observed k_t ($J_{pred}(k_t^{obs})$)

$\beta = 1/18.6$ were used to calculate the solid line in Fig. 8B, and dotted lines correspond to the predicted $k_t/(u_* Sc^{-2/3})$ in the confident interval of $f = (9.7 \pm 1.4) \times 10^{-3}$. The skill score of the prediction of $k_t/(u_* Sc^{-2/3})$ with Eq. 13 is $ss = 0.81$, and the correlation coefficient $r = 0.93$. In Fig. 8b, marks $+$ indicates predicted $k_t/(u_* Sc^{-2/3})$ using variable friction coefficient computed with Eq. 7.

Figure 8C test the performance of estimating J with Eq. 18 and the computed k_t with Eq. 13, $\beta = 1/18.6$ and $f = 9.7 \times 10^{-3}$ (called as $J_{pred}(k_t^{pred})$). Figure 8c shows a good agreement between observed and predicted DO fluxes across the WSI ($ss = 0.85$, and the correlation coefficient $r = 0.95$). However, of J is computed with the observed transfer velocity ($J_{pred}(k_t^{obs})$), the difference between $J_{pred}(k_t^{obs})$ and $J_{pred}(k_t^{pred})$ is small, which indicates that the flux across the WSI in the experiments is controlled by biochemical uptake of DO in the sediments, rather than by k_t (see [11, 12], and Eq. 19).

4.4 Validation with field measurements

The transferability of Eq. 13 was tested against the field measurements that were presented by de la Fuente [11]. The measurements were obtained during a two day field campaign

that was conducted in Salar del Huasco (20.274°S, 68.883°W, 3800 m above sea level) in northern Chile. Salar del Huasco is a Chilean national park that is also protected by the Convention on Wetlands of International Importance (Ramsar Convention). Most of the aquatic ecosystem is sustained by benthic primary production that occurs in surface sediment that are reddish-brown and soft organic mud of a few millimeters thick, while deep sediments are dark muddy sediments, whose odor indicated that anoxic reactions occur. Thickness of the photosynthetic active layer where benthic primary production occurs was 1 mm during windy conditions and anoxic conditions were observed 1 to 2 mm below the WSI.

Diurnal atmospheric cycles in the lagoon are characterized by calm conditions during the morning and windy conditions in the afternoons between 13 and 19 h, when wind-induced waves govern the hydrodynamics of the lagoon [11]. Turbulence and mass transport during calm conditions is driven by convection induced by over-heating of the surface layer of sediments [11]. The field measurements were performed at a location where the water was approximately 5 cm deep and varied from 2.5 to 10 cm deep as a result of the tilting of the free surface in response to the opposing pressure gradient. During the field campaign, one standard Campbell meteorological station recording every 30 s was installed approximately 50 m from the study site. The wind shear velocity shown in Fig. 9a was computed from the measured wind speed and the Charnock parameterization of the
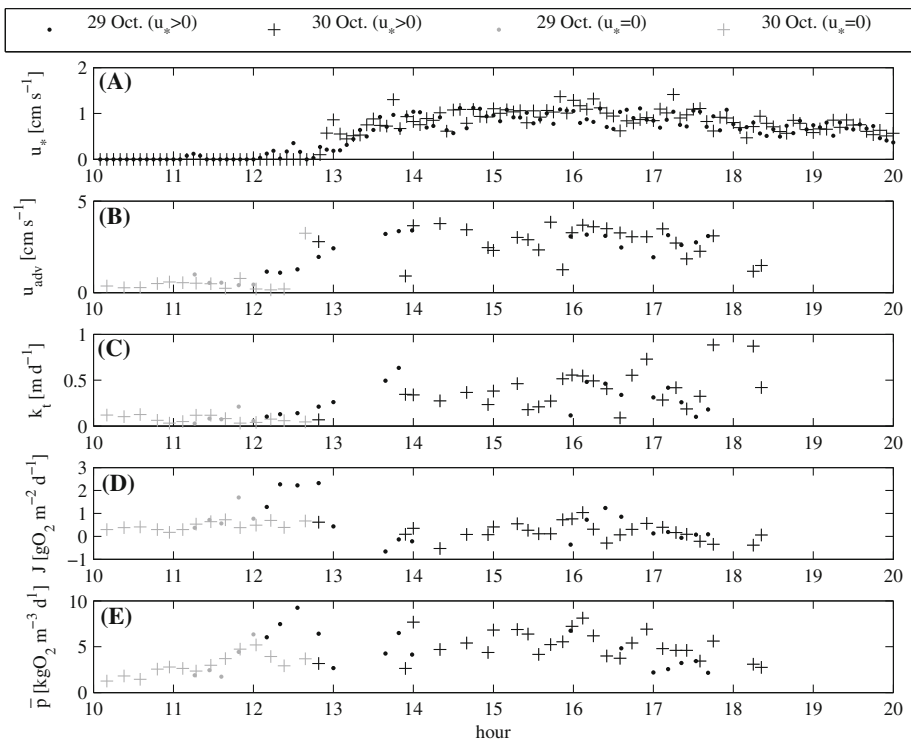

Fig. 9 Observations in Salar del Huasco [11]. Time series of: a wind-shear velocity, b Reynolds number, c k_t, d J and E) average rate of DO production in the sediments ($\bar{p}$). Marks *plus* indicate observations in 29 of October 2013, dots observations during 30 of October 2013. *Black marks* are observations with wind speed, and *grey marks* during calm conditions

water dynamic roughness [7, 15]. Furthermore, time series of the flow velocity were measured with the 2D side-view ADV used in the laboratory experiment (Fig. 9b). Measurements marked with light grey corresponds to observation during calm conditions where turbulence and mass transport was explained in free convection produced by over-heating of the surface layer of the sediments (see [11]). In addition, the water temperature was recorded with an Onset Tidbit temperature data logger, and the Schmidt number varied between 375 and 625 in response to changes in water temperature between 16 and 26 °C. Although that changes in Schmidt number were important, changes in other variables were also large as well experimental error in field observations, thus making difficult to properly isolate the influence of water temperature on k_t. Finally, a total of 43 DO micro-profiles during windy conditions are available for assessing the diffusional mass transfer coefficient (Fig. 9c) and J (Fig. 9d). These micro-profiles were obtained with the OX-25 microprobe connected to a Microsensor Multimeter Unisense signal amplifier mounted on a gauge set on a tripod. The micro-profiling process for obtaining k_t is the same than the methodology used in this article, and is detailed in de la Fuente [11]. It is important to notice that J in the field campaign was dominated by benthic primary production ($J > 0$ in Fig. 9d means that DO flows from the sediments to the atmosphere). The average rate of DO production in the photosynthetic active layer ($\bar{p}$) is shown in Fig. 9e, where it is observed a temporal variation depending on the water temperature and solar radiation [11]. Thickness of the diffusive boundary layer varied between 0.5 and 3.5 mm, and was measured by setting the vertical spacing of the microprofile to 0.16 mm.

Based on the previous measurements, the coefficient α was computed by fitting the flow velocity computed with Eq. 4 at the ADV elevation to the field observations. This method provides one coefficient α for every micro-profile (Fig. 10a). With the coefficient α, the vertical average velocity U was computed by integrating Eq. 4, and the obtained value was in average 60 % larger than the measured flow speed with the ADV (Fig. 10b). Following the same experimental procedure as in the laboratory, the bulk friction coefficient was computed as it is shown in Fig. 10c, obtaining $f = (7 \pm 0.6) \times 10^{-3}$. Finally, Fig. 10D plots $k_t/(u_* Sc^{-2/3})$ as a function of the Reynolds number, where the solid line corresponds to the predicted $k_t/(u_* Sc^{-2/3})$ using Eq. 13, $\beta = 1/18.6$ and $f = 7 \times 10^{-3}$, while dotted lines were drawn based on the confidence intervals of $\beta = 1/(18.6 \pm 5.1)$ and $f = (7 \pm 0.6) \times 10^{-3}$. The correlation coefficient was 0.48, and a p value < 0.01 was obtained between the observed values of $k_t/(u_* Sc^{-2/3})$ and Re^{-1}, which indicates that both variables are more likely to be related by a physical process than a random correlation. Marks with + corresponds to the predicted $k_t/(u_* Sc^{-2/3})$ with friction coefficients calculated with Eq. 7.

Finally and similarity than for laboratory experiments, processes in both sides of the WSI are required for testing the performance of Eq. 13 in estimating J. In the case of field observations in Salar del Huasco, benthic primary production produced that during most part of the day, DO flowed from the sediments toward the water column (Fig. 9d). The conceptual model of Ordoñez et al. [29] was used to include this source of DO in the computation of J. This conceptual model requires rates of DO production and uptake in the sediments that were measured by de la Fuente [11], and a shape parameter that accounts for the heterogeneity of rate of DO production in the sediments. Following Ordoñez et al. [29], the shape parameter for field observations was equal to 1.012 ± 0.04 (not shown, $ss = 0.91$, $r = 0.96$) which indicates that the primary production was mostly uniform in the photosynthetic active layer (see [29] for further information). The comparison between observed and predicted J is shown in Fig. 11. The accuracy of this prediction was good ($ss = 0.81$, $r = 0.95$); however, as same as for the laboratory experiments, J computed
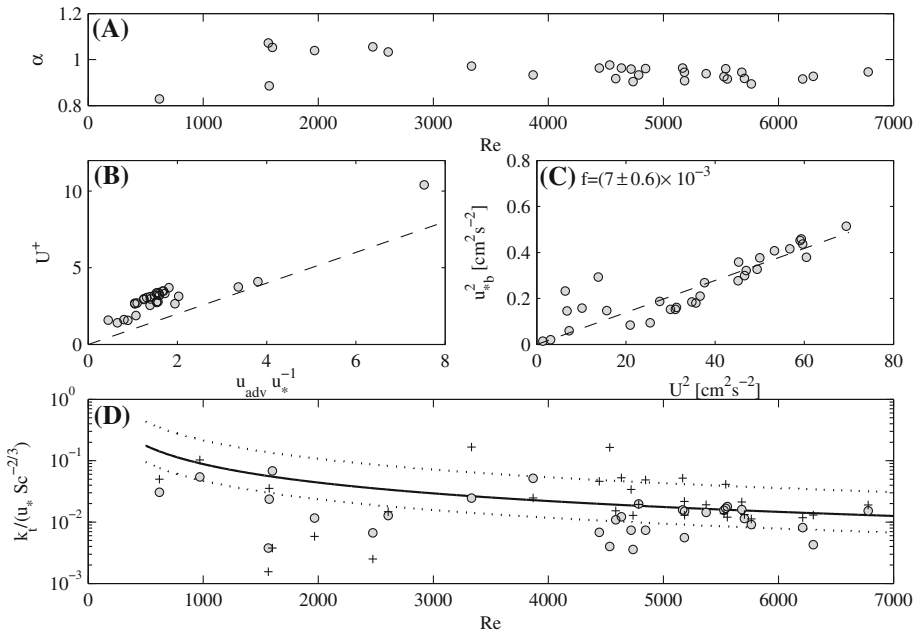
Fig. 10 **a** Fitted coefficient α as function of the Reynolds number. **b** Comparison between average flow velocity U and measured velocity with the ADV, u_{ADV}. **c** Comparison between square of the bottom shear velocity and U^2. The slope corresponds to the bottom friction coefficient (Eq. 7). **d** Validation of Eq. 13 based on the field observations. *Grey circles* correspond to direct measurements of $k_t/(u_*Sc^{-2/3})$ as function of the Reynolds number. *Solid line* to the predicted $k_t/(u_*Sc^{-2/3})$ using Eq. 13 and constant friction coefficient of 7×10^{-3} of **c**; and marks *plus* correspond to the predicted $k_t/(u_*Sc^{-2/3})$ computed with Eq. 13 and friction coefficients of Eq. 7

Fig. 11 Comparison between observed and predicted J using conceptual model of Ordoñez et al. [29] and using predicted k_t with Eq. 13 ($J_{pred}(k_t^{pred})$) and observed k_t ($J_{pred}(k_t^{obs})$)
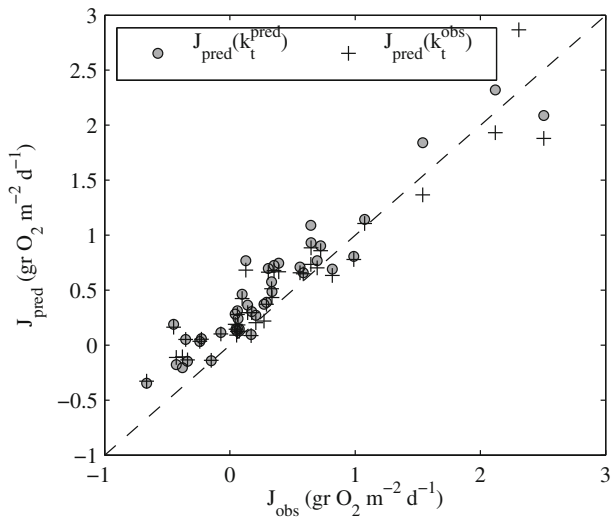
with predicted and observed k_t provides similar values, which indicates that J was primarily dominated by processes in the sediments.

5 Discussion

Laboratory experiments were conducted to obtain a relationship to predict the diffusional mass transfer coefficient at the WSI in a very shallow flow that is driven by the wind. By introducing a turbulent closure for the eddy viscosity, an analytical expression for the vertically-averaged wind-induced flow velocity as a function of the viscous sub-layer thickness, friction coefficient, horizontal pressure gradient, wind-shear velocity and Reynolds number was obtained (Eq. 13). The assumption that the diffusive sub-layer thickness is proportional to the viscous sub-layer thickness (Eq. 9) was required to use Eq. 13 to compute the diffusional mass transfer coefficient as a function of the flow properties. Equation 13 was obtained and shows that both the wind shear velocity and the Reynolds number of the wind-induced flow are needed to predict k_t. The validity of Eq. 13 was also successfully tested using the field observations of Fig. 10d. The differences between the field observations and the predicted values can be attributed to several factors, including the unsteady nature of the field conditions and the role of wind-induced waves.

In contrast to open channel flow over a smooth surface, the viscous sub-layer thickness in terms of the surface units (z_0^+) is not constant and varied from 1.8 to 7.8 with an average value of $z_0^+ = 4.3$ (see Table 1). The values of h^+ varied from 145 to 1170, which justified the assumption of $z_0^+ << h^+$ that is required to obtain Eq. 13. In other words, $z_0^+ << h^+$ implies that the flow is fully turbulent. However, it is important to recall the hydraulic conditions that led to Eq. 13: it was derived in the laboratory for Reynolds numbers of the wind induced current between 500 and 3500, and validated in the field for Reynolds numbers that reached values of 10^5.

The ADV measurements showed that the influence of wind-induced waves near the bottom can be neglected. However, as was described in (de la Fuente [11]), the hydrodynamics during windy conditions in the field are governed by wind-induced waves that explain the sediment resuspension that is observed in the afternoons. Waves also drive pressure gradients that induce vertical velocities in submerged sediments [3]. Despite this, Eq. 13 predicted both the order of magnitude of k_t and the inverse relationship with the Reynolds number of the wind-induced current. It is important to recall that a p value of 0.01 was obtained between the observed values of $k_t/(u_* Sc^{-2/3})$ and Re^{-1}, which means that that observed changes in $k_t/(u_* Sc^{-2/3})$ are more likely to be explained in terms of Re^{-1} than by an random process.

The theoretical approach required two parameters, β and f, that have very different meanings: β is the ratio between the thickness of the diffusive boundary layers and z_0 (Figs. 7a), where z_0 represents the elevation at which the logarithmic velocity profile is 0, while f is the friction coefficient that is required to compute the bottom shear stress as a function of the wind-induced current (Fig. 7b, c). Our measurements indicate that f can be considered constant and independent of the wind-induced flow (RE, h, u_*). Two similar characteristic values of f were obtained in the laboratory ($f = 1 \times 10^{-2}$) and the field (7×10^{-3}).

Finally, the performance of using Eq. 13 to compute J was also tested using both laboratory and field observations. This validation was done by considering that J depends on processes that occur in both sides of the WSI [11, 12, 26, 29]. Given this perspective of

the problem, the good prediction of J was observed in the laboratory and the field. However, in both sets of observations the value of J was primarily dominated by processes of DO uptake/production in the sediments, rather than by turbulent transport across the diffusive boundary layer. In this way, the error in the estimation of k_t is not entirely transferred to the calculus of J. As a consequence, the estimation of J requires correct quantification of processes in both sides of the WSI. In the water-side of the WSI, the diffusional mass transfer coefficient for a very shallow flow that is induced by the wind can be computed using Eq. 13. The bottom friction coefficient for this wind-induced flow varies in the range of $(7\text{--}10) \times 10^{-3}$.

References

1. Boudreau BP, Jørgensen BB (2001) The benthic boundary layer: transport processes and biogeo-chemistry. Oxford University Press, Oxford
2. Brand A, Dinkel C, Wehrli B (2009) Influence of the diffusive boundary layer on solute dynamics in the sediments of a seiche-driven lake: a model study. J Geophys Res 114:G01010. doi:10.1029/2008JG000755
3. Brennen CE, Imberger J (2014) The wave-induced solute flux from submerged sediment. Environ Fluid Mech 14:221–234. doi:10.1007/s10652-013-9307-2
4. Bryant L, Lorrai C, McGinnis D, Brand A, Wüest A, Little J (2010) Variable sediment oxygen uptake in response to dynamic forcing. Limnol Oceanogr 55:950–964
5. Bryant L, McGinnis D, Larrai C, Brand A, Little J, Wüest A (2010) Evaluating oxygen fluxes using microprofiles from both sides of the sediment–water interface. Limnol Oceanogr Methods 8:610–627
6. Bouldin DR (1968) Methods for describing the diffusion of oxygen ando ther mobile constituents across the mud–water interface. J Ecol 56:77–87
7. Csanady GT (2004) Air–sea interaction. Cambridge University Press, Cambridge
8. Dade WB (1993) Near-bed turbulence and hydrodynamic control of diffusional mass transfer at the sea floor. Limnol Oceanogr 38:52–69
9. Dade WB, Hogg AJ, Boudreau BP (2001). Physics of flow above the sediment-water interface. Pages 4–43 of: Gualtieri C, Mihailovic DT (eds), Fluid mechanics of environmental interfaces. Taylor & Francis
10. de la Fuente A, Niño Y (2010) Temporal and spatial features in the thermo-hydrodynamics of a shallow salty lagoon in Northern Chile. Limnol Oceanogr 55:279–288
11. de la Fuente A (2014) Heat and dissolved oxygen exchanges between the sediment and water column in a shallow salty lagoon. J Geophys Res Biogeosci 119:596–613. doi:10.1002/2013JG002413
12. de la Fuente A (2015) Methodology for analyzing dissolved oxygen consumption in benthic chambers. J Environ Eng 141:04014098
13. Dejoux C (1993) Benthic invertebrates of some saline lakes of the SudLipez region, Bolivia. Hydro-biologia 267:257–267
14. Fischer H, List E, Koh R, Imberger J, Brooks N (1979) Mixing in inland and coastal waters. Academic Press, New York
15. Garratt JR (1992) The atmospheric boundary layer. Cambridge University Press, Cambridge
16. Glud RN, Berg P, Fossing H, Jørgensen BB (2007) Effect of the diffusive boundary layer on benthic mineralization and O-2 distribution: a theoretical model analysis. Limnol Oceanogr 52:547–557
17. de Herrera V, Gregori I, Pinochet H (2009) Assessment of trace elements and mobility of arsenic and manganese in lagoon sediments of the salars of Huasco and Coposa, Chilean Altplano. J Chil Chem Soc 54:1565
18. Higashino M, Stefan H (2012) Model of turbulence penetration into a suspension layer on a sediment bed and effect on vertical solute transfer. Environ Fluid Mech 12:451–469
19. Hondzo M, Feyaerts T, Donovan R, O'Connor BL (2005) Universal scaling of dissolved oxygen distribution at the sediment–water interface: a power law. Limnol Oceanogr 50:1667–1676
20. Jørgensen B, Revsbech N (1985) Diffusive boundary layers and the oxygen uptake of sediment and detritus. Limnol Oceanogr 30:111–122

21. Kampf S, Tyler S, Ortiz C, Muñoz J, Adkins P (2005) Evaporation and land surface energy budget at the Salar de Atacama, Northern Chile. J Hydrol 310:236–252
22. Kühl M, Jørgensen BB (1992) Microsensor measurements of sulfate reduction and sulfide oxydation in compact microbial communities of aerobic biofilms. Appl Environ Microbiol 58:1164–1174
23. Lorke A, Muller B, Maerki M, Wuest A (2003) Breathing sediments: the control of diffusive transport across the sediment-water interface by periodic boundary-layer turbulence. Limnol Oceanogr 48(6):2077–2085
24. Magnaudet J, Thais L (1995) Orbital rotational motion and turbulence below laboratory wind water waves. J Geophys Res 100:757–771
25. Murphy AH (1988) Skill Scores based on the mean square error and their relationships to the correlation coefficient. Mon Weather Rev 116:2417–2424
26. Nakamura Y, Stefan HG (1994) Effect of flow velocity on sediment oxygen demand: theory. J Environ Eng 120:996–1016
27. Nezu I, Nakagawa H (1993). Turbulence in Open-Channel Flows.Balkema
28. O'Connor BL, Hondzo M (2008) Dissolved oxygen transfer to sediments by sweep and eject motions in aquatic environments. Limnol Oceanogr 53(2):566
29. Ordoñez C, de la Fuente A, Díaz P (2015) Modeling the influence of benthic primary production on oxygen transport through the water–sediment interface. Ecol Model 311:1–10
30. Rasmussen H, Jørgensen BB (1992) Microelectrode study of seasonal oxygen uptake in a coastal sediment: role of molecular diffusion. Mar Ecol Prog Ser 81:289–303
31. Revsbech N, Jørgensen B, Brix O (1981) Primary production of microalgae in sediments measured by oxygen microprofile H14CO3-fixation, and oxygen exchange methods. Limnol Oceanogr 26:717–730
32. Spigel R, Imberger J (1980) The classification of mixed-layer dynamics in lakes of small to medium size. J Phys Oceanogr 10:1104–1121
33. Steinberger N, Hondzo M (1999) Diffusional mass transfer at sediment-water interface. J Environ Eng 125:192–200
34. Thais L, Magnaudet J (1996) Turbulent structure beneath surface gravity waves sheared by the wind. J Fluid Mech 328:313–344
35. Williams W, Carrick T, Bayly I, Green J, Berbst D (1995) Invertebrates in salt lakes of the Bolivian Altiplano. Int J Salt Lakes Res 4:65–77
36. Zuñiga LR, Campos V, Pinochet H, Prado B (1991) A limnological reconnaissance of Lake Tevenquiche, Salar de Atacama Chile. Hydrobiologia 210:1–2